Reconstructing physiological oxygen gradients reveals the role of hypoxia in colon epithelial organization

Jiaquan Yu[1,*], Chuyi Chen[1*], Felicia H. Rodriguez[1,2], Gianfranco L. Yee[1,2], Isabella Y. Zeng[1,2], Kevin Yang[1], Elizabeth K. Benitez[3,4], Karuna Ganesh[3,5+], and Scott R. Manalis[1,2,5,6,7+]

Affiliations
[1]Koch Institute for Integrative Cancer Research, Massachusetts Institute of Technology, 500 Main St building 76, Cambridge, MA 02139, USA
[2]Department of Biological Engineering, Massachusetts Institute of Technology, 21 Ames St #56-651, Cambridge, MA 02139, USA
[3]Molecular Pharmacology Program, Sloan Kettering Institute, Memorial Sloan Kettering Cancer Center, New York, NY 10065, USA
[4]Weill Cornell/Rockefeller/Sloan Kettering Tri-Institutional MD-PhD Program, New York, NY 10065, USA
5Department of Medicine, Memorial Sloan Kettering Cancer Center, New York, New York 10065, USA
[6]Broad Institute of Harvard and MIT, 415 Main St, Cambridge, MA 02142, USA
[7]Department of Mechanical Engineering, Massachusetts Institute of Technology, 33 Massachusetts Ave, Cambridge, MA 02139, USA

* Authors contributed equally
+Corresponding authors: srm@mit.edu and ganeshk@mskcc.org

Abstract

Oxygen gradients organize tissue architecture and metabolism[1,2], yet their precise spatial profiles and mechanistic roles remain poorly understood because both *in vivo* measurement and *in vitro* control are technically challenging[3,4]. Here, we quantify the oxygen landscape of the mammalian intestine using microscale sensors, revealing a steep luminal–basal gradient of approximately 10-60 μM mm⁻¹ that collapses under antibiotic perturbation. We then recreate this physiological range *ex vivo* with a submerged chemostat microfluidic platform that fixes the oxygen boundary condition by coupling an oxygen-permeable PDMS chip to an external scavenger reservoir and integrating embedded optical sensors for real-time readout. This architecture suppresses ambient oxygen ingress and sustains programmable gradients of 10-20 μM mm⁻¹ across three-dimensional colorectal cancer organoid cultures while remaining compatible with live imaging and endpoint retrieval. The platform bridges quantitative *in vivo* oxygen mapping with controlled *ex vivo* modeling, establishing a generalizable approach to interrogate how spatial oxygen dynamics govern epithelial organization and disease progression.

Introduction

Oxygen gradients are fundamental to tissue physiology, guiding development, metabolism, and adaptation[5]. In the intestine, oxygen declines sharply from the arterioles in the submucosa to the mucosal surface, shaping epithelial polarity and microbial ecology[6,7]. Although absolute oxygen levels have been measured in several organs[8], the spatial derivatives that define gradient steepness and continuity remain poorly characterized[2]. This lack of quantitative gradient information obscures whether disruptions in oxygen distribution directly modulate intestinal physiology and cancer progression.

Three-dimensional human organoids derived from healthy donors or patient tumors provide powerful models for epithelial biology and disease. Yet these cultures typically experience uniform oxygenation far exceeding physiological levels, because ambient oxygen readily diffuses through polymers and media[9–11]. Efforts to impose hypoxia, using materials with low oxygen diffusivity and gas-controlled incubators, have achieved partial success but are limited by instability, lack of quantitative control, and incompatibility with live imaging [12,13]. A platform that can stably reproduce *in vivo* gradients while enabling direct measurement and visualization would close this critical gap.

Here, we introduce a scavenger-submerged microfluidic chemostat that overcomes these limitations. By immersing a PDMS chip in a heated oxygen-scavenger bath and a confined microfluidic oxygen supply, the device maintains a precise oxygen boundary condition at the chip level. This setup eliminates ambient leakage, permits placement of embedded optical oxygen sensors within 200 μm of the culture, enables real-time oxygen readout, and supports multi-day 3D organoid culture under physiologically relevant gradients, without specialized incubators. We then show that this system reconstructs intestinal oxygen landscapes across defined microfluidic geometries, linking *in vivo* measurements to tunable *ex vivo* environments.

Results

To define the native oxygen landscape of the intestine, we performed microsensor-based measurements in the large intestine of euthanized C57BL/6 mice under normoxic conditions. After dissection, a needle-encapsulated trace-range electrode was advanced along the colonic lumen. In wildtype mice, luminal oxygen remained <2 μM distal to the cecum and throughout the colon, whereas antibiotic-treated mice, characterized by epithelial inflammation and depletion of commensal microbiota, exhibited significantly elevated luminal oxygen with a mean of 40 μM (**Fig. 1a**). Together with published values (**Extended Data Table 1**), these data indicate that a substantial luminal-to-basal oxygen difference is a hallmark of colon physiology and collapses when the homeostasis is disrupted.

To determine the actual oxygen gradient and enable human–mouse comparison, we analyzed histological sections from a CRC patient (KG146P) and previous reports (**Extended Data Table 1**). By measuring the distance from the mucous surface to adjacent vasculature and integrating published intratumoral oxygen measurements, we estimated that maximum *in vivo* human CRC cancer gradient is 30 μM mm^{-1} (**Fig. 1b**). Although *ex vivo* organoids recapitulate key aspects of tumor architecture (**Fig. 1c**), their oxygen profiles diverge markedly. Specifically, finite-element simulations (COMSOL) indicate that external gradients above 10 μM mm^{-1}, when imposed across epithelial structures, dominate intrinsic oxygen consumption, driving directional oxygen fluxes that are non-centrosymmetric (**Fig. 1d,e**). Together, these results underscore that the key feature of 30 μM mm^{-1} oxygen gradient *in vivo* has yet to be reconstructed and tested *ex vivo*.

Building on the physiological oxygen gradients quantified *in vivo*, we next sought to recreate oxygen profiles *ex vivo* using a controllable microfluidic system. To build such a chemostat culture platform, we leveraged the oxygen permeability of polydimethylsiloxane (PDMS) to develop a submerged microfluidic culture chip capable of generating physiologically relevant oxygen gradients (**Fig. 2a**). This approach directly addresses the limitations of previous methods and provides two distinct advantages.

First, submerging the chip in a heated, oxygen-scavenger–filled tank prevents ambient oxygen exchange (**Extended Data Note 1**). This configuration eliminates the need for hypoxia incubators[14] while allowing an oxygen sensor system and bright-field imaging to be fully integrated on-chip (**Extended Data Fig. 1a**). Taking advantage of the accessibility of the submerged design, we embedded a customized, high-sensitivity oxygen sensor strip within the PDMS channel and positioned less than 200 μm away from the ECM and organoids (**Extended Data Fig. 1b**). A fiber-optic probe continuously scans the sensor strip to read localized oxygen concentration in real time (**Fig. 2a, Extended Data Fig. 2a**), generating complete oxygen profiles every seven minutes (**Extended Data Fig. 2b**).

Second, by placing the scavenger outside the PDMS chip and introducing on-chip oxygen source and scavenger sink channels, we achieved stable, physiologically relevant oxygen levels and gradients (**Fig. 2b–e**). Notably, both empirical measurements (**Fig. 2b**) and COMSOL simulations (**Extended Data Note 2**) revealed that the scavenger-submerged configuration is essential to achieve physiological hypoxia. Without the submerged scavenger, oxygen concentrations exceed 100 μM within 500 μm of the on-chip sink (**Extended Data Note 2**), a limitation previously reported for devices lacking ambient isolation[13].

Confining the oxygen source within the chip while surrounding it with a liquid scavenger as an external sink enables precise control over oxygen gradients through three key design features. First, the simplicity of the design allows oxygen gradients to be generated in a wide variety of microfluidic configurations, provided that an oxygen source channel is incorporated[15,16]. For example, we fabricated four- and five-channel chips with varying culture-channel dimensions and source-to-culture distances, each producing distinct oxygen gradient profiles (**Extended Data Fig. 3b,c**). Second, separating the oxygen source channel from the cell-culture channels with a PDMS barrier enables gas exchange without direct liquid contact[17]. This configuration allows the use of either mixed gas or air-saturated water as the oxygen source (**Fig. 2c**) and permits independent flow-rate control in the source channel without imposing shear stress on the cultured cells (**Fig. 2d, Extended Data Fig. 3a**). Finally, water flow rates can be controlled with much greater precision than airflow, and the slower diffusion rate of oxygen in water allows finer control over hypoxic conditions[18]. Hypoxia establishes in the tank within one minute (**Extended Data Note 1**), and adjustable oxygen gradients in the range of 30 μM to 120 μM form across the culture region within one hour (**Fig. 2b,c; Extended Data Note 2**).

Because the sodium sulfite–based scavenger reacts with oxygen faster than oxygen can diffuse into the liquid, it effectively prevents oxygen from reaching the culture region (**Extended Data Note 1**). Stability was maintained until the scavenger was fully neutralized, a process mitigated by replacing the scavenger every two days (**Fig. 2e, Extended Data Note 1**). This approach not only produces robust and reproducible oxygen gradients but also supports long-term studies of oxygen-dependent biological processes in 3D organoid cultures.

The ability to precisely map oxygen gradients across a 3D organoid culture in the chemostat enables direct correlation between oxygen levels and organoid behavior (**Extended Data Fig. 4a,b**). Using bright-field imaging, we spatially annotated individual organoids according to their position within the gradient (**Fig. 2f**), quantifying both absolute oxygen levels (in μM) and gradient steepness (in $\mu M\ mm^{-1}$). The system ensures stable oxygen conditions with less than 5 % variation (**Extended Data Fig. 4c**) across the 10 mm culture region (X-axis) and yields more than ten organoids per oxygen level per chip. Together, these features provide a practical and generalizable platform for reconstructing physiological oxygen gradients *ex vivo*, linking quantitative *in vivo* measurements to tunable, stable microenvironments for mechanistic studies of 3D tissue organization.

In colorectal cancer (CRC), tumor progression is closely aligned to the oxygen gradient along the luminal-basal axis of the intestinal epithelium[19]. CRC typically originates from intestinal stem cells at the base of colonic crypts, initially forming polyps that protrude into the hypoxic intestinal lumen[20,21]. Such hypoxia-associated polyps can cause bleeding and obstruction, but are benign and can be endoscopically resected, preventing progression to cancer[22]. As polyps progress to cancer, they invade basally, accessing oxygen-carrying blood vessels, and from there, disseminate to distant sites[23]. Migration along this apical-basal oxygen gradient is therefore a key prognostic and predictive feature of CRC, yet the specific role of the oxygen gradient in driving polarity reversal in CRC cells has not been previously studied due to the lack of physiological *ex vivo* culture systems[24]. Like the normal colon, CRC and patient-derived CRC organoids self-organize into polarized structures with F-actin-bounded apical lumen and an ECM-facing basal layer[25]. A primary tumor consists of multiple such glandular epithelial “organoid”-like structures encapsulated in ECM and stroma, and organized along the apical-basal oxygen gradient of the intestine (**Extended Data Fig. 5**). Mechanical disruption, such as physical dissection or transitioning from ECM to suspension culture, can induce reorganization, altering the apical-basal orientation[25]. This polarity coexists with an intrinsic oxygen gradient: higher oxygen levels on the basal (ECM and capillary facing) side and hypoxic conditions on the apical (luminal) side[26].

Leveraging our chemostat platform’s ability to generate stable and precisely tunable oxygen gradients, we investigated a key question: how does growth in an oxygen gradient, in comparison with hypoxia *per se*, influence CRC polarity and morphology? Studying this distinction is challenging because cellular oxygen consumption naturally generates oxygen gradients (luminal hypoxia/basal high oxygen from media) as organoids grow, complicating efforts to isolate and analyze these effects. Using our platform, we established a controlled environment to systematically test how hypoxia versus oxygen gradients influence CRC architecture (**Extended Data Fig. 6a,b**).

Since there are no reported measurements of oxygen gradients in 3D *ex vivo* organoid cultures, we first sought to estimate how external oxygen gradients influence the intrinsic luminal/basal gradients established by cellular oxygen consumption. Using COMSOL simulations, we modeled an external, *in vivo*-like oxygen gradient that disrupted the centrosymmetric oxygen profile, creating a non-centrosymmetric trans-organoid gradient (**Fig. 3a, Extended Data Fig. 6a**). Initially, we simulated oxygen gradients generated solely by intrinsic cellular consumption. Due to the absence of reported oxygen consumption values for organoids under hypoxic conditions, we relied on literature-derived estimates to model a range of possible oxygen gradients. In all scenarios, intrinsic oxygen profiles remained centrosymmetric, with a hypoxic core exceeding 48 μM. Next, we incorporated an external oxygen gradient resembling physiological *in vivo* conditions, such as those achievable using the chemostat system (**Extended Data Fig. 6b**). Simulations of a 200 μm diameter organoid with a 50 μm shell thickness, corresponding approximately to a single-cell layer, revealed that external gradients on the order of 10-20 μM mm⁻¹ significantly disrupted the intrinsic oxygen consumption pattern. Notably, the external gradient reversed the direction of oxygen flux at the hypoxic side, driving oxygen from the organoid core toward the luminal surface. These findings highlight the critical role of externally applied gradients in overriding the centrosymmetric gradient driven by cellular consumption and reshaping oxygen profiles within tissues.

Numerous studies have reported how hypoxia influences the polarization and differentiation of CRC, particularly through pathways regulated by HIF-1α[27]. We thus hypothesized that the intrinsic centrosymmetric oxygen profile plays a pivotal role in governing organoid growth and shape through classical hypoxia-driven mechanisms involving HIF-1[28]. To examine the influence of hypoxia, we transduced patient-derived CRC organoid KG146P[29] with a UnaG reporter which encodes 5 copies of the hypoxia response element directing the expression of a destabilized oxygen-independent fluorescent protein (dUnaG) [30,31]. UnaG transfected organoids displayed negligible autofluorescence under ambient oxygen conditions but reliably exhibit green fluorescence in hypoxic culture. When cultured under uniform hypoxic conditions at 50μM oxygen, the KG146P organoids uniformly expressed UnaG, representing global HIF-1 activation (**Fig 3b**). However, when exposed to a mild oxygen gradient averaging 50 μM, even with a minimal oxygen difference (<2 μM) across the organoid, we observed polarized UnaG expression, with higher signal intensity localized to the hypoxic side.

Interestingly, this disruption of the centrosymmetric oxygen profile was associated with inward growth of the organoids, with gradual filling of the organoid lumens (**Fig 3c**). This inward growth process commenced after ~12 hours of oxygen gradient culture and progressed until the lumen was no longer visible. Both mouse intestinal stem cell-derived and primary patient-derived CRC organoids displayed intraluminal growth (**Fig. 3c**). In patient-derived KG146P CRC organoids exposed to oxygen levels below 50 μM, 91.6% of individual organoids showed a significant reduction in lumen size over 48 hours (**Fig. 3e**) accompanied by an increase in cell-covered area (**Fig. 3f**), yielding a net expansion in overall organoid volume that mirrors the luminal filling, proliferation, and biomass accumulation characteristic of tumors *in vivo*[32]. Organoids can be maintained in chemostat for over a week with continued growth, allowing assessment of reversibility of the luminal filling phenotype. Remarkably, reverting oxygen gradient back to normoxia fully restored the original cystic morphology of KG146P CRC organoids within 48 hours (**Extended Data Fig. 7**). These findings demonstrate that the external oxygen gradient can act to dynamically and reversibly sculpt epithelial architecture, inducing luminal filling and epithelial overgrowth that are characteristic hallmarks of tumorigenesis.

We next asked whether oxygen gradient-induced morphological changes are associated with cytoskeletal rearrangements and alterations in epithelial cell polarity and stemness. The chemostat chips, with the PDMS layer mounted on a glass coverslip, are compatible with conventional confocal microscopy (**Extended Data Fig. 1b**). Following two days of culture under a 30 μM mm⁻¹ oxygen gradient, organoids were fixed *in situ* to prevent readaptation, and their apical-basal organization was analyzed using confocal microscopy. We first asked whether induction of an oxygen gradient plays a role in organizing the stem-differentiation axis of the intestinal epithelium by transducing mouse intestinal organoids with the Stem Cell ASCL2 Reporter (STAR)[33]. In mouse intestinal stem cell organoids expressing the STAR reporter, oxygen gradient exposure led to a spatial location-specific loss of stem cell gene expression in the most hypoxic part of the gradient where the oxygen flux was reversed by the external gradient (**Fig. 3d**). This observation suggests that the oxygen gradient likely plays a role in inducing the differentiation gradient observed in the normal intestine, where stem cells normally reside at the (most oxygenated) base of intestinal crypts. Phalloidin staining of F-Actin confirmed that both mouse normal and human cancer organoids grown under uniform 50 μM hypoxia exhibited typical apical-basal polarization, characterized by a dense, smooth apical (luminal) F-actin layer. However, when exposed to an external oxygen gradient, this actin layer appeared twisted, disorganized, and redistributed across both the apical and basal sides of the organoids (**Fig. 3d**).

In contrast, CRC primary tumor organoids, which are epigenetically restricted to an intestinal stem cell state[34], retained STAR expression regardless of the oxygen gradient. However, approximately 20% of the CRC organoids developed a compact, no-lumen morphology during prolonged culture, in which the apical F-actin lining was disrupted and redistributed internally (**Fig. 3d**). Since active migration is associated with mitochondrial localization between the cell nucleus and F-actin in the direction of migration[35], we stained CRC patient organoids with Mitotracker FM Deep Red, DAPI, and F-Actin to visualize relative location of mitochondria, nucleus and polarity, respectively. Staining of CRC primary organoids fixed 36 hours after exposure to the oxygen gradient revealed mitochondria concentrated around the actin structures, in between the nucleus and apical lining actin, which is consistent with the directionality of active migration toward the actin-aligned filling lumen (**Fig. 4a**). Importantly, the compact morphology and apically concentrated mitochondria induced by chemostat-generated oxygen gradients closely mirror the histology of the cognate tumor tissue from patient KG146P. Within the same tumor, glandular structures containing regions of evenly distributed mitochondria and regions of apically polarized mitochondria towards the lumen are detectable **(Fig. 4b)**. These disease-relevant morphological features, which are absent in organoids grown under standard normoxia but can be induced by culture in oxygen gradients in the chemostat, implicate the physiological oxygen gradient of the intestine as an important driver of the luminal filling, migration and dense growth that are characteristic of cancer progression in the clinic. To further extend the chemostat platform from single-organoid phenotypes to tissue-level reconstruction, we dissociated CRC organoids and seeded them against the ECM interface to generate continuous epithelial layers under controlled oxygen gradients **(Fig. 4c)**. Within six days, these fragments compacted into a cohesive tissue that could be tracked in real time by bright-field imaging, enabling longitudinal analysis of growth dynamics in the chemostat **(Fig. 4d,e)**. Fixed tissues stained for F-actin revealed heterogeneous lumen sizes within the continuous layer **(Fig. 4f)**, closely resembling the duct-like variability observed in patient tumor histology (**Extended Data Fig. 5**).

Discussion

Contemporary microfluidic hypoxia platforms are often custom engineered, requiring bespoke integration of oxygen sensors, fluidics and imaging components[36–38]. To address these limitations, we established a set of design principles, developed a modular integration framework, and assembled a catalog of commercially available components that enable the generation of precise oxygen gradients in PDMS-based microfluidic systems. This approach provides a practical and reproducible pathway for enhancing chip-based platforms with tunable oxygen control.

Our modular system, combining an external scavenger reservoir with embedded PDMS-integrated sensors, can be readily adapted for applications ranging from organotypic culture and cell sorting to chemical synthesis and multi-omic assays. From a biological perspective, we show that spatial oxygen gradients, rather than uniform hypoxia, are key regulators of colorectal cancer organoid morphology and polarity associated with invasive tumor behavior. These findings highlight the importance of re-evaluating the role of hypoxia in cancer biology, developmental processes, and tissue physiology, specifically distinguishing the effects of oxygen gradient dynamics from those of absolute oxygen concentration.

Acknowledgements

We thank Dr. Arnold Levine, Dr. Dan Littman, and Dr. Matthew Vander Heiden for helpful discussions and Annie Chen for facilitating device fabrication. This work was supported by Stand Up To Cancer (SU2C) Convergence Program 3.1416, D. K. Ludwig Fund for Cancer Research, and the MIT Center for Precision Cancer Medicine. This work was also supported in part by the Koch Institute Support (core) Grant P30-CA014051 from the National Cancer Institute.

Competing interests

The authors disclosed no competing interest.

Figures:

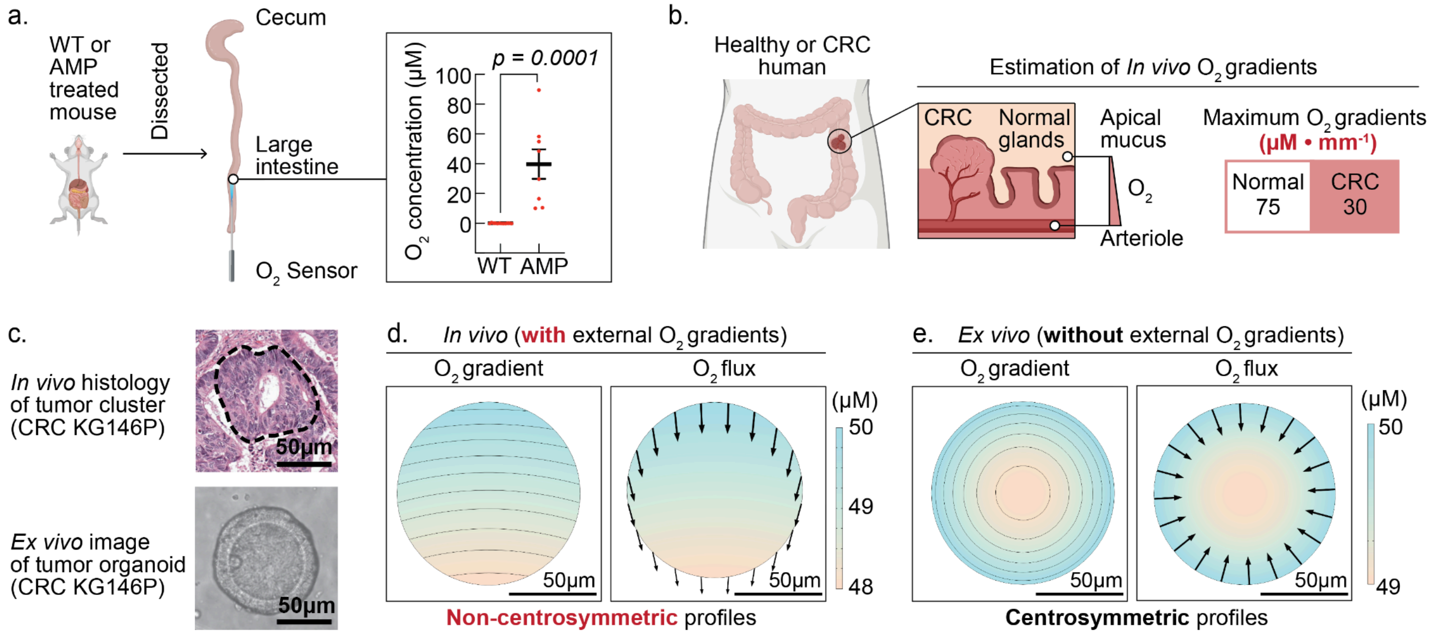

Fig. 1| *Ex vivo* organoid culture exhibits a different oxygen profile than *in vivo* tissue. a. *In vivo* measurement of oxygen levels in mouse intestine; **b.** Estimated maximum oxygen gradient ranges for healthy and CRC humans; **c.** Histology of CRC patient KG146P showing ductal architecture cancer *in vivo*, shown in black circles. 3D grown *ex vivo* organoids from KG146P recapitulates the *in vivo*-like cystic architectures; **d.** Simulated *in vivo* oxygen concentration profile showing non-centrosymmetric oxygen profiles; **e.** Simulated oxygen concentration profile of *ex vivo* grown KG146P organoids showing that oxygen profiles differ significantly from *in vivo* to *ex vivo* conditions, even when maintained at stable ambient hypoxia of 50 μM.

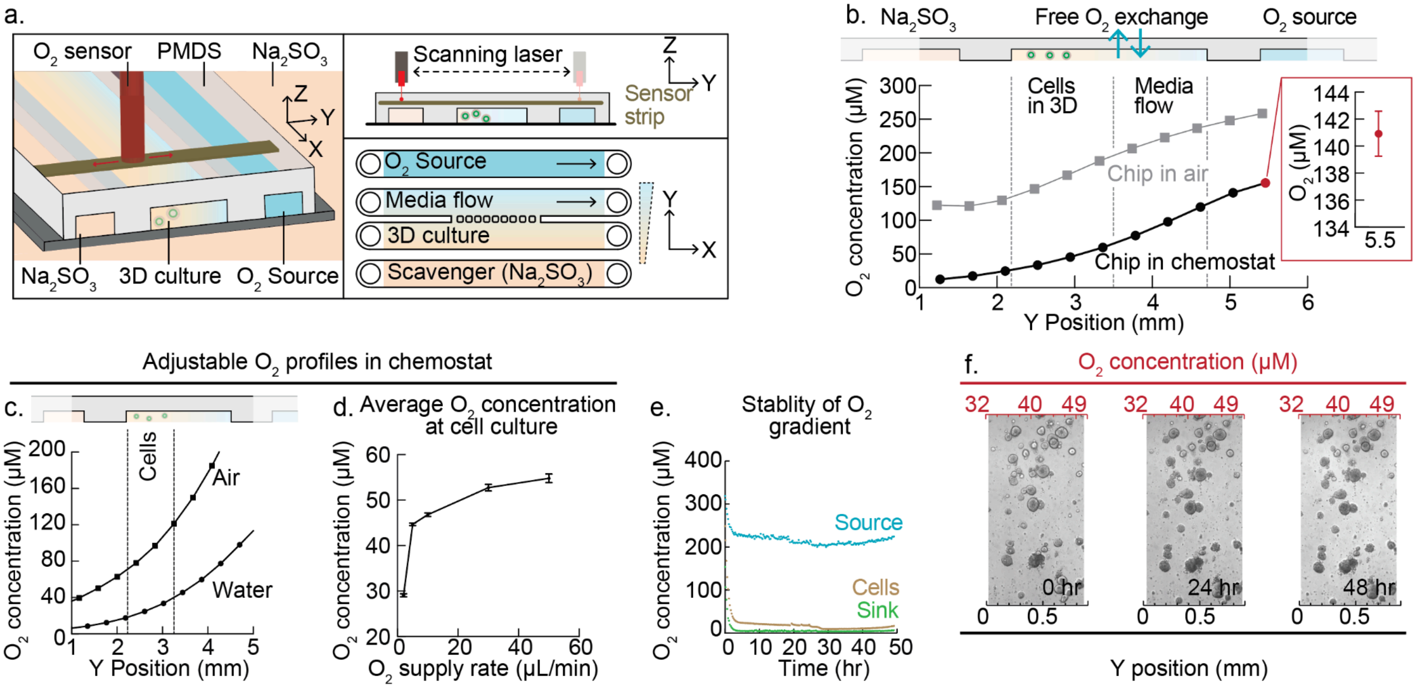

Fig. 2| Chemostat system to maintain colorectal cancer organoids with stable trans-organoid oxygen gradients. a. Schematic of the chemostat comprising a four-channel PDMS chip submerged under sodium sulfite oxygen scavenger, integrated with an oxygen-scanning sensor and time-lapse microscopy to profile stable oxygen gradients across 3D cultures; **b.** Measured oxygen profiles demonstrating that scavenger submergence is required to achieve physiologically relevant intestinal hypoxia; **c and d.** Tunable oxygen gradients (20–120 µM) across the cell culture region achieved by varying **(c)** oxygen source and **(d)** flow rate of oxygen source (air saturated water); **e.** Continuous real-time tracking of oxygen concentration over 50 hours showing gradient stability using air-saturated water as oxygen source at a flow rate of 2 µl/min.; **f.** Combined oxygen scanning and time-lapse microscopic imaging, enabling quantitative mapping of oxygen levels and gradients across individual organoids from patient KG146P.

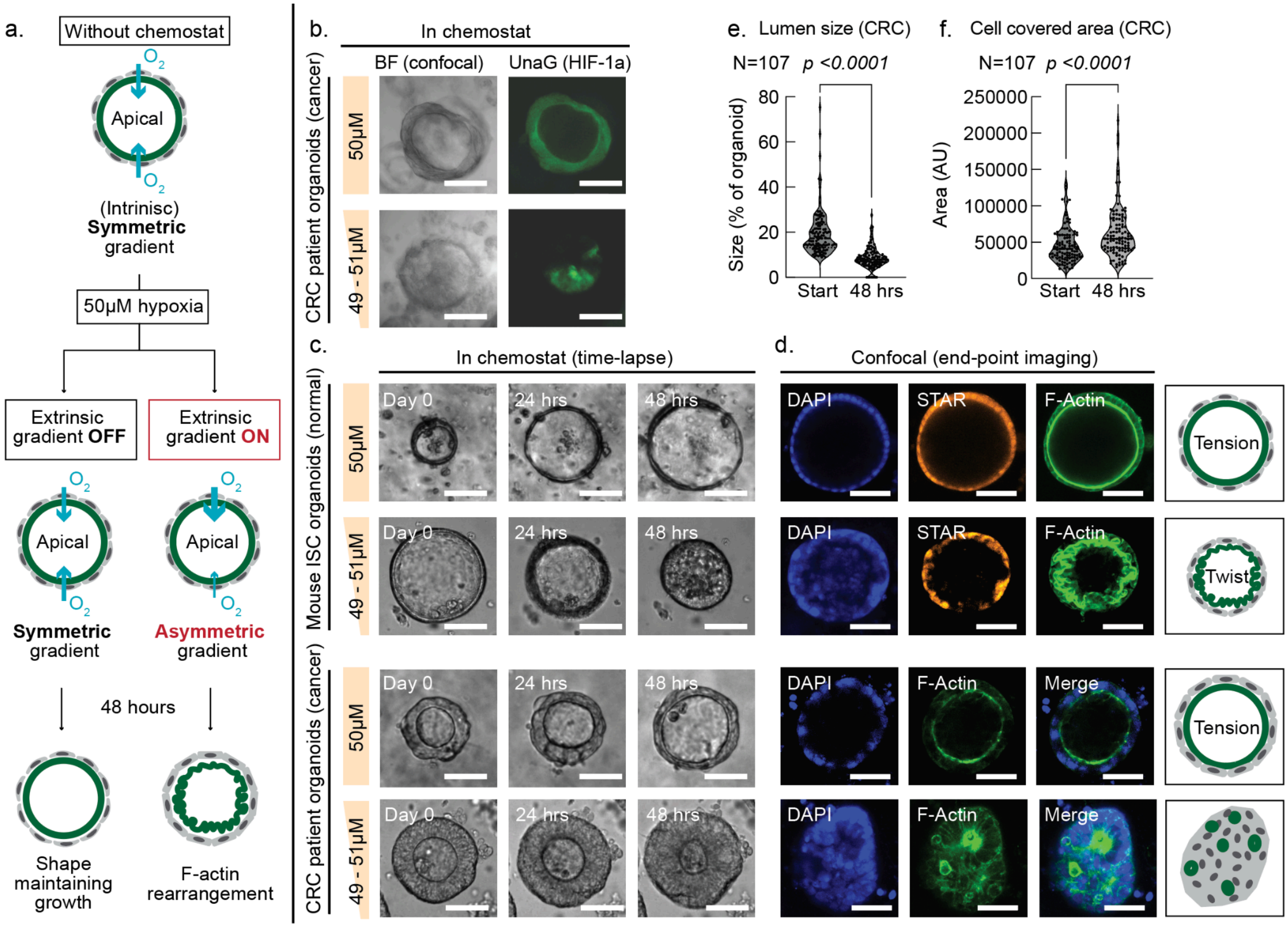

Fig. 3| Oxygen gradients govern colorectal organoid architecture. a. Schematic illustrating how an imposed oxygen gradient induces polarity reversal and F-actin rearrangement in patient-derived CRC organoids; **b.** Fluorescence images of patient-derived CRC organoids expressing the UnaG hypoxia reporter under uniform hypoxia or an imposed oxygen gradient, showing even UnaG signal distribution under uniform conditions and its concentration on the hypoxic side under a gradient; **c.** Bright-field images from the chemostat chip showing outward (cystic) growth under uniform hypoxia versus inward (compact) growth under an oxygen gradient; **d.** Confocal micrographs depicting organoid morphology under uniform hypoxia compared to hypoxic-gradient culture; **e.** Quantification of inward growth under an oxygen gradient as a reduction in lumen size over 48 h; **f.** Quantification of cell-covered area under an oxygen gradient over 48 h; **e,f.** P values from paired two-tailed t-tests with Welch's correction; **b.c.d.** Scale bars are 100μm.

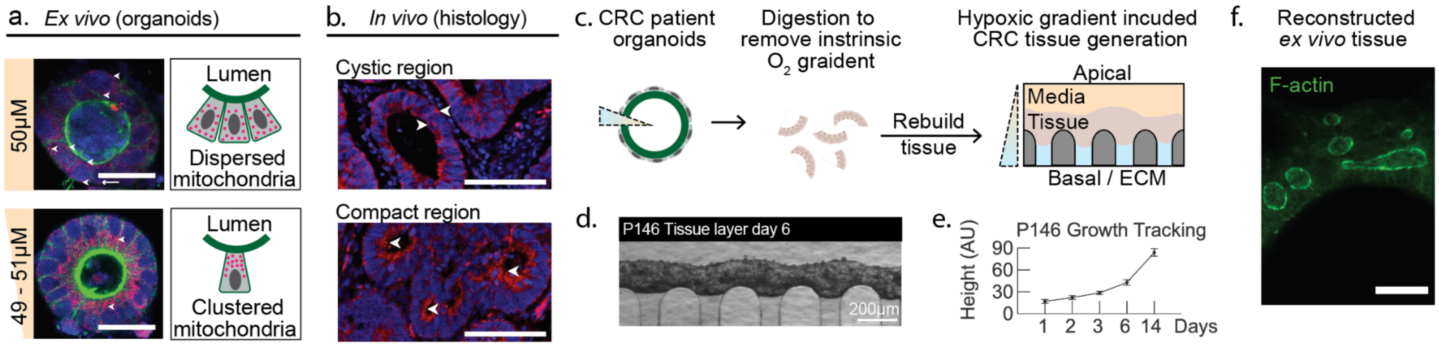

Fig. 4 | Hypoxia-induced tissue compaction enables reconstruction of *ex vivo* CRC tissue with histological heterogeneity. a. Patient-derived CRC organoids cultured under chemostat-generated oxygen gradients show mitochondrial clustering (red) on the apical side of nuclei (blue). **b.** Immunofluorescence of patient tumor KG146P tissue sections stained for TOMM20 (red) and DAPI (blue) reveals regions with dispersed mitochondria (top) and regions with apically polarized mitochondria (bottom), echoing the *ex vivo* phenotype. **c.** Schematic illustrating reconstruction of CRC tissue under imposed oxygen gradients, following digestion of organoids to remove intrinsic oxygen profiles. **d.** Bright-field image showing continuous epithelial tissue formed after 6 days of chemostat culture. **e.** Real-time imaging enables longitudinal tracking of tissue growth in the chemostat. **f.** F-actin staining highlights heterogeneous lumen sizes within reconstructed tissue, resembling patient histology. **a,b,f.** Scale bars, 100 μm. d, scale bar, 200 μm.

References:

1. Moore, M., Moore, R. & McFetridge, P. S. Directed oxygen gradients initiate a robust early remodeling response in engineered vascular grafts. *Tissue Eng. Part A* **19**, 2005–2013 (2013).
2. Ardakani, A. G., Cheema, U., Brown, R. A. & Shipley, R. J. Quantifying the correlation between spatially defined oxygen gradients and cell fate in an engineered three-dimensional culture model. *J. R. Soc. Interface* **11**, 20140501 (2014).
3. Marassi, V. *et al.* The challenges of O2 detection in biological fluids: Classical methods and translation to clinical applications. *Int. J. Mol. Sci.* **23**, 15971 (2022).
4. Icha, J., Weber, M., Waters, J. C. & Norden, C. Phototoxicity in live fluorescence microscopy, and how to avoid it. *Bioessays* **39**, (2017).
5. Grant, J. *et al.* Establishment of physiologically relevant oxygen gradients in microfluidic organ chips. *Lab Chip* **22**, 1584–1593 (2022).
6. Albenberg, L. *et al.* Correlation between intraluminal oxygen gradient and radial partitioning of intestinal microbiota. *Gastroenterology* **147**, 1055–63.e8 (2014).
7. Taylor, S. R. *et al.* Dietary fructose improves intestinal cell survival and nutrient absorption. *Nature* **597**, 263–267 (2021).
8. Zheng, L., Kelly, C. J. & Colgan, S. P. Physiologic hypoxia and oxygen homeostasis in the healthy intestine. A Review in the Theme: Cellular Responses to Hypoxia. *Am. J. Physiol. Cell Physiol.* **309**, C350–60 (2015).
9. Carreau, A., El Hafny-Rahbi, B., Matejuk, A., Grillon, C. & Kieda, C. Why is the partial oxygen pressure of human tissues a crucial parameter? Small molecules and hypoxia. *J. Cell. Mol. Med.* **15**, 1239–1253 (2011).
10. Wenger, R. H., Kurtcuoglu, V., Scholz, C. C., Marti, H. H. & Hoogewijs, D. Frequently asked questions in hypoxia research. *Hypoxia (Auckl.)* **3**, 35–43 (2015).
11. Pavlacky, J. & Polak, J. Technical feasibility and physiological relevance of hypoxic cell culture models. *Front. Endocrinol. (Lausanne)* **11**, 57 (2020).
12. Chen, Y.-A. *et al.* Generation of oxygen gradients in microfluidic devices for cell culture using spatially confined chemical reactions. *Lab Chip* **11**, 3626–3633 (2011).
13. Lam, S. F., Shirure, V. S., Chu, Y. E., Soetikno, A. G. & George, S. C. Microfluidic device to attain high spatial and temporal control of oxygen. *PLoS One* **13**, e0209574 (2018).
14. Rexius-Hall, M. L., Rehman, J. & Eddington, D. T. A microfluidic oxygen gradient demonstrates differential activation of the hypoxia-regulated transcription factors HIF-1α and HIF-2α. *Integr. Biol. (Camb.)* **9**, 742–750 (2017).
15. Lorenzo-Martín, L. F. *et al.* Spatiotemporally resolved colorectal oncogenesis in mini-colons ex vivo. *Nature* **629**, 450–457 (2024).
16. Zhao, Y. *et al.* Integrating organoids and organ-on-a-chip devices. *Nat. Rev. Bioeng.* **2**, 588–608 (2024).
17. Xu, L., Lee, H., Jetta, D. & Oh, K. W. Vacuum-driven power-free microfluidics utilizing the gas solubility or permeability of polydimethylsiloxane (PDMS). *Lab Chip* **15**, 3962–3979 (2015).
18. of Air Content on the Oxygen Diffusion Coefficient wang#s:TopTitleof Growing Mediawang#e:TopTitle. **4**, (2013).
19. Saxena, K., Jolly, M. K. & Balamurugan, K. Hypoxia, partial EMT and collective migration: Emerging culprits in metastasis. *Transl. Oncol.* **13**, 100845 (2020).
20. Barker, N. *et al.* Crypt stem cells as the cells-of-origin of intestinal cancer. *Nature* **457**, 608–611 (2009).
21. Klos, C. L. & Dharmarajan, S. Polyp genetics. *Clin. Colon Rectal Surg.* **29**, 289–295 (2016).
22. Mathews, A. A., Draganov, P. V. & Yang, D. Endoscopic management of colorectal polyps: From benign to malignant polyps. *World J. Gastrointest. Endosc.* **13**, 356–370 (2021).
23. Wang, J.-D. *et al.* The histologic features, molecular features, detection and management of serrated polyps: a review. *Front. Oncol.* **14**, 1356250 (2024).
24. Chen, K., Collins, G., Wang, H. & Toh, J. W. T. Pathological Features and Prognostication in Colorectal Cancer. *Curr. Oncol.* **28**, 5356–5383 (2021).
25. Co, J. Y., Margalef-Català, M., Monack, D. M. & Amieva, M. R. Controlling the polarity of human gastrointestinal organoids to investigate epithelial biology and infectious diseases. *Nat. Protoc.* **16**, 5171–5192 (2021).
26. Wang, Y. *et al.* Bioengineered Systems and Designer Matrices That Recapitulate the Intestinal Stem Cell Niche. *Cellular and molecular gastroenterology and hepatology* **5**, (2018).

27. Cao, D. *et al.* Expression of HIF-1alpha and VEGF in colorectal cancer: association with clinical outcomes and prognostic implications. *BMC Cancer* **9**, 1–9 (2009).
28. Masoud, G. N. & Li, W. HIF-1α pathway: role, regulation and intervention for cancer therapy. *Acta Pharm. Sin. B.* **5**, 378–389 (2015).
29. Moorman, A. *et al.* Progressive plasticity during colorectal cancer metastasis. *Nature* **637**, 947–954 (2024).
30. Sattiraju, A. *et al.* Hypoxic niches attract and sequester tumor-associated macrophages and cytotoxic T cells and reprogram them for immunosuppression. *Immunity* (2023) doi:10.1016/j.immuni.2023.06.017.
31. Erapaneedi, R., Belousov, V. V., Schäfers, M. & Kiefer, F. A novel family of fluorescent hypoxia sensors reveal strong heterogeneity in tumor hypoxia at the cellular level. *EMBO J* **35**, 102–113 (2016).
32. Murray, G. F. *et al.* Live cell mass accumulation measurement non-invasively predicts carboplatin sensitivity in triple-negative breast cancer patient-derived xenografts. *ACS Omega* **3**, 17687–17692 (2018).
33. Oost, K. C. *et al.* Specific Labeling of Stem Cell Activity in Human Colorectal Organoids Using an ASCL2-Responsive Minigene. *Cell Rep* **22**, 1600–1614 (2018).
34. Yang, C. *et al.* Tumor organoid model of colorectal cancer (Review). *Oncol. Lett.* **26**, 328 (2023).
35. Desai, S. P., Bhatia, S. N., Toner, M. & Irimia, D. Mitochondrial localization and the persistent migration of epithelial cancer cells. *Biophys J* **104**, 2077–2088 (2013).
36. Azimzadeh, M. *et al.* Microfluidic-based oxygen (O2) sensors for on-chip monitoring of cell, tissue and organ metabolism. *Biosensors (Basel)* **12**, 6 (2021).
37. Ando, Y. *et al.* A microdevice platform recapitulating hypoxic tumor microenvironments. *Sci. Rep.* **7**, 15233 (2017).
38. Grist, S. M., Schmok, J. C., Liu, M.-C. A., Chrostowski, L. & Cheung, K. C. Designing a microfluidic device with integrated ratiometric oxygen sensors for the long-term control and monitoring of chronic and cyclic hypoxia. *Sensors (Basel)* **15**, 20030–20052 (2015).

Extended data:

Reconstructing physiological oxygen gradients reveals the role of hypoxia in colon epithelial organization

Jiaquan Yu[1,*], Chuyi Chen[1*], Felicia H. Rodriguez[1,2], Gianfranco L. Yee[1,2], Isabella Y. Zeng[1,2], Kevin Yang[1], Elizabeth K. Benitez[3,4], Karuna Ganesh[3,5+], and Scott R. Manalis[1,2,5,6,7+]

Affiliations
[1]Koch Institute for Integrative Cancer Research, Massachusetts Institute of Technology, 500 Main St building 76, Cambridge, MA 02139, USA
[2]Department of Biological Engineering, Massachusetts Institute of Technology, 21 Ames St #56-651, Cambridge, MA 02139, USA
[3]Molecular Pharmacology Program, Sloan Kettering Institute, Memorial Sloan Kettering Cancer Center, New York, NY 10065, USA
[4]Weill Cornell/Rockefeller/Sloan Kettering Tri-Institutional MD-PhD Program, New York, NY 10065, USA
5Department of Medicine, Memorial Sloan Kettering Cancer Center, New York, New York 10065, USA
[6]Broad Institute of Harvard and MIT, 415 Main St, Cambridge, MA 02142, USA
[7]Department of Mechanical Engineering, Massachusetts Institute of Technology, 33 Massachusetts Ave, Cambridge, MA 02139, USA

* Authors contributed equally
+Corresponding authors: srm@mit.edu and ganeshk@mskcc.org

Extended Data Table 1

1.1 Overview: Using Oxygen Scavenger to Enable Hypoxia Culture

Condition	Length scale (mm)	Reference	Location	O_2 Concentration Range (μM)	Reference	Maximum O_2 Gradient (μM mm^{-1})
Human (Healthy)	0.7 to 1.4	1 - 3	Arteriole	5 - 60	4, 5	75
			Lumen	6 - 14	5, 6	
Human (CRC)	1.4 to 3.9 (Measured)	KG146P	Arteriole	14 - 42	6, 7	30
			Lumen	4 - 15	8	
Mouse (Healthy)	0.2 to 0.5 (Measured)	9	Arteriole	56 - 60	4, 6	250
			Lumen	10 - 22	4	
Mouse (Disease)	0.2 to 0.3 (Measured)	10	Arteriole	25 - 75	4	315
			Lumen	12 - 40	4	

*Maximum oxygen gradient was defined as the largest arteriole–lumen oxygen difference divided by the shorter length scale, with values rounded to the nearest 5-unit increment.

Extended Data Note 1

1.1 Overview: Using Oxygen Scavenger to Enable Hypoxia Culture

To establish and maintain a hypoxic environment for organoid culture, we designed a submerged tank system filled with a sodium sulfite (Na_2SO_3) solution, which functions as a chemical oxygen scavenger. The tank was constructed as a cuboid with internal dimensions of 8 × 11 × 8 cm^3, yielding a total volume of approximately 700 mL. The sodium sulfite actively reacts with dissolved molecular oxygen, limiting ambient oxygen diffusion into the surrounding medium and the embedded microfluidic chip. The relevant reaction proceeds via:

$$2\ Na_2SO_3 + O_2 \rightarrow 2\ Na_2SO_4.$$

We performed matched COMSOL simulations and experimental measurements to characterize two key phases of this oxygen-quenching process. In the initial phase, addition of sodium sulfite to oxygen-saturated water rapidly depletes dissolved oxygen, creating a uniformly hypoxic aqueous environment. Over subsequent days, oxygen levels remain near zero as the scavenger continues to neutralize oxygen diffusing in from the ambient air. Our simulation and empirical results consistently demonstrate that, as long as an adequate concentration of scavengers is maintained, the system sustains hypoxia throughout the culture period. Our findings are corroborated by numerical predictions, experimental data, and previously reported values from the literature, collectively validating the use of this submerged scavenger design for mutil-day hypoxic culture.

1.2 Governing Equation and Parameters

Since there is no convective flow in the tank, the profile of oxygen concentration C governed by the following diffusion-reaction equation:

$$\frac{\partial C}{\partial t} = D\nabla^2 C + R \tag{1}$$

For the initial phase of oxygen quenching, the reaction term R_o is pseudo first order [11] as:

$$R_o = -k_o C \tag{2}$$

And for the subsequent scavenger quenching phase:

$$R_s = -k_s C_s^{0.65} \tag{3}$$

D is the oxygen diffusion coefficient in sodium sulfite solution, k_o and k_s are the reaction rate constants representing oxygen consumption by the sodium sulfite, C_s is the sodium sulfite concentration, and t is the time. The equation for R is determined by multiple studies demonstrating that the rate of the uncatalyzed oxidation of sodium sulfite in aqueous solution is independent of the dissolved oxygen concentration, indicating a reaction order of zero with respect to oxygen. The same studies report that the reaction rate depends on the sodium sulfite concentration, with the reaction experimentally determined to be approximately 0.65th order [12,13]. The critical parameters used in the simulation are shown in **Table 1** below:

Parameter	Value	Basis for Selection
Microfluidic chip position	The center of the microfluidic chip is located at point P with coordinates of (4 cm, 5.5 cm, 1 cm) within the tank	The position aligns with the information in **Extended Data Fig. 1a**.

Oxygen diffusion coefficient in sodium sulfite	$\sim 2.75\times 10^{-9}\ m^{2}/s$	Oxygen diffusion in sodium sulfite solution is approximated to that in water[14]
Oxygen solubility in water	$210\ \mu mol/L$	Approximate saturation concentration in sodium sulfite solution at around physiological temperature [15]
Oxygen concentration in air	20.95% $(\sim 8.56\times 10^{-3}\ mol/L)$	Oxygen concentration in air at room temperature calculated by the Ideal Gas Law; used as the ambient boundary condition
Initial sodium sulfite concentration	$4.26\ \ g/L$ $(\sim 33.8\ \times 10^{-3} mol/L)$	Reflects the experimental setup. The sodium sulfite concentration was intentionally set at this high level to minimize the need for solution replacement and prevent disturbance to long-term organoid culture
Pseudo first order sodium sulfite–oxygen reaction rate constant, k_o	$0.048\ \ s^{-1}$,$0.19\ s^{-1}$	Various values considered based on literature [11]
Sodium sulfite–oxygen reaction rate constant, k_s	$3\times 10^{-5} mM^{0.35}/s$, $5.77\times 10^{-5} M^{0.35}/s$, $1.23\times 10^{-5} M^{0.35}/s$	Various values considered based on literature[12,13]

Table 1 | Constants used to simulate scavenger reaction.

We assumed that at t = 0, the concentration of oxygen in the tank is $10^{-3}\ mol/L$ (saturated) everywhere, and at y = 0 cm and y = 8 cm, the concentration is always $2.1\times 10^{-4}\ mol/L$. Since the tank is air permeable, we assumed that oxygen diffuses into the tank freely.

1.3 Numerical Model Setup

1.3.1 Hypoxia can be established in chemostat within a minute

We modeled the system in COMSOL and solved for the oxygen concentration at point P over time, and found that the oxygen level falls below detection (to ~ 0μM) after 39 seconds using the best-fit reaction rate constants, corresponding to the oxygen sensor data obtained from the Chemostat that indicates complete oxygen quenching within 35-40 seconds. (**Extended Data Note 1 Fig. 1**).

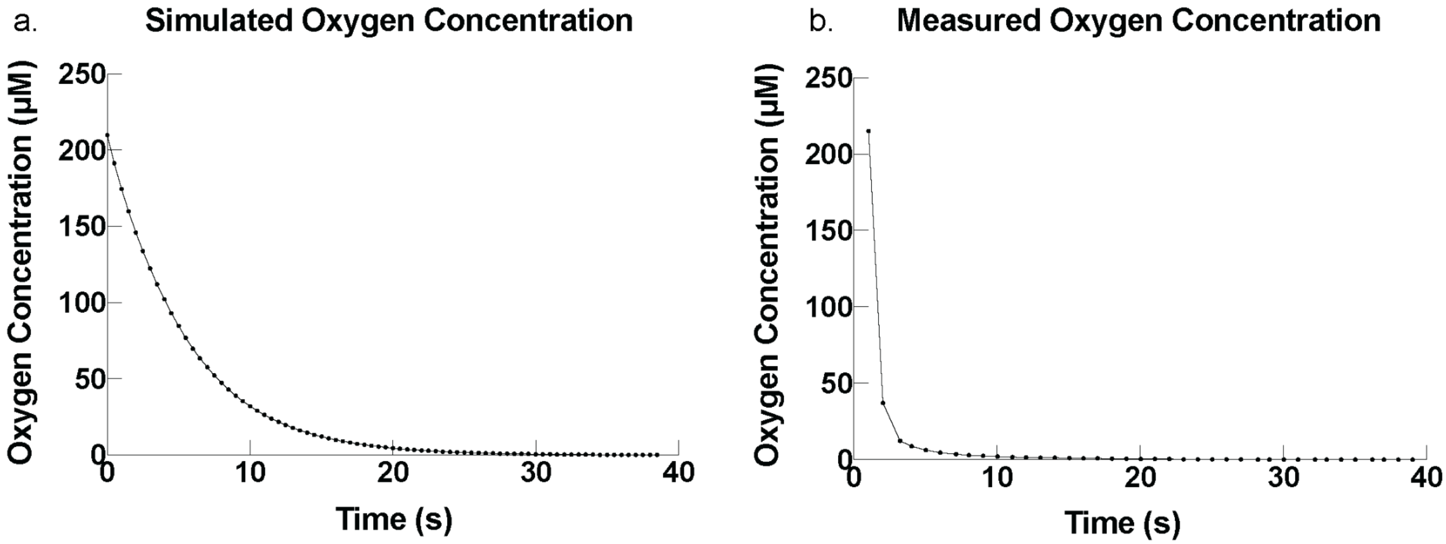

Extended Data Note 1 Fig. 1 | Hypoxia in the chemostat can be established rapidly. a. COMSOL simulation yields zero oxygen level at the center of the microfluidic chip (x=4 cm, y=5.5 cm, z=1 cm) within 39 seconds using the oxygen scavenger tank. **b.** The simulation is verified by the oxygen profile obtained using the oxygen sensor and the chemostat system, upper bounding the oxygen quenching time to 40 seconds. The first 20 seconds were used for adding the sodium sulfite into the solution, and temporarily stirring the solution to achieve a uniform scavenger concentration. The time needed in the empirical experiment for establishing a uniform concentration likely contributed to the delay of oxygen concentration drop and caused a sharper slope.

1.3.2 Hypoxia can be maintained without addition of scavenger for >3 days

The corresponding COMSOL simulation was used to estimate the quenching time of the oxygen scavenger. All parameters and tank geometry were as previously described. Additional considerations include:

- A 1 cm-thick plastic tank wall was modeled in COMSOL. However, its impact on the quenching profiles is negligible due to the high oxygen diffusivity.
- At the surface of the tank, the oxygen concentration boundary condition was set to $210\ \mu M$, representing 20.95% of oxygen's solubility in water in the absence of reaction. This adjustment reflects the dominance of the rapid reaction over diffusion, which maintains the oxygen concentration at a significantly lower level than its equilibrium solubility.

The rate constant $k_s = 1.23\times10^{-5} M^{0.35}/s$ provided the best agreement with empirical data, yielding a scavenger quenching time of 100-110 hours. In the first 48 hours, the scavenger concentration remains above 6 μM. For approximately 4 days, the concentration of oxygen scavenger stays positive and the oxygen level remains at zero **(Extended Data Note 1 Fig. 2a)**, indicating that hypoxic conditions are stably sustained throughout this period. The simulation aligns with the oxygen concentration profile from the chemostat **(Extended Data Note 1 Fig. 2b)**.

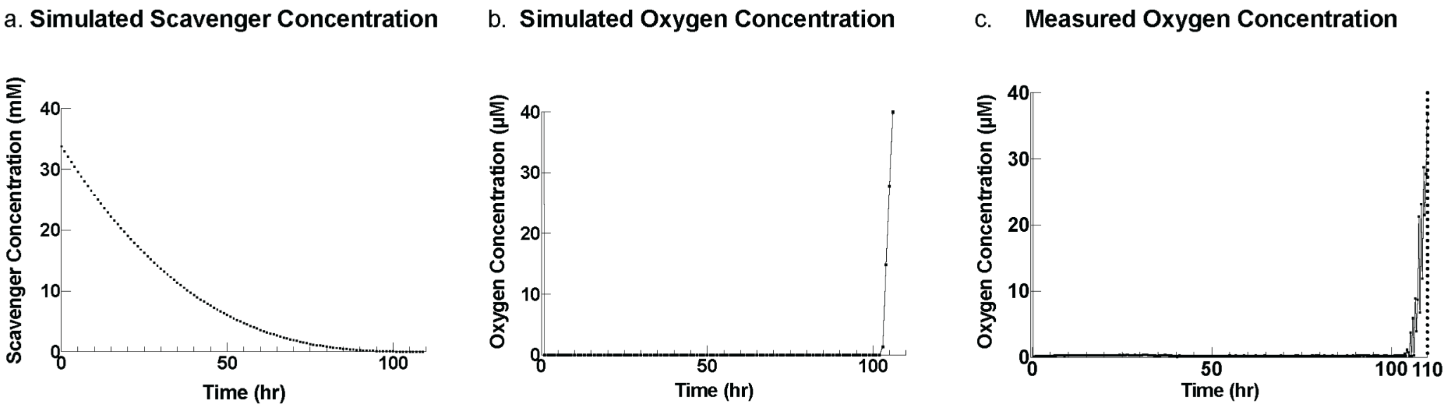

Extended Data Note 1 Fig. 2 | Hypoxia in the chemostat can be established quickly and maintained over days. a&b. The sodium sulfite concentration (averaged) in the tank shows that a positive amount of scavenger is consuming oxygen for more than 96 hours (4 days), resulting in complete oxygen depletion for 102 hours, and a subsequent oxygen level increase. **b.** Chemostat data agrees with the numerical analysis, showing a zero oxygen level within the first 100 hours, and a steep oxygen concentration rebound around the 100th-110th hours, aligning with the simulated time point for the scavenger quenching.

Extended Data Note 2
Modeling Oxygen Transport and Gradients in the Microfluidic Chip

To investigate oxygen concentration distribution within the microfluidic chip, a three-dimensional model was developed using finite element method (FEM)-based computational modeling software COMSOL Multiphysics (Burlington, MA, USA) [16]. The simulation domain consists of a PDMS block (15 x 25 x 4 mm³) housing the channels measuring 0.25 mm in height and 1.5 mm in width, bonded to a glass substrate at the bottom (**Extended Data Note 2 Fig. 1a**). The flow within channels was modeled using the "Laminar Flow" interface. The "inlet" conditions were applied to channel inlets with specified flow rates, and the "outlet" conditions were applied to the ends of the channels, with the pressure set to zero. The boundary conditions were set to "no slip" wall at the bottom, top, and sides of the channels. The flow within the channels was solved by a "stationary" solver. The "Transport of Diluted Species in Porous Media" interface was used to simulate oxygen diffusion through the PDMS, governed by Eqn. (1) (**Extended Data Note 1**). The oxygen concentrations in both the oxygen source and scavenger channels were assumed to be constant by applying a fixed value using a "Concentration" node. The oxygen concentration at the PDMS surface was assumed to be zero, as the chip was fully submerged in an excess of scavenger solution. The oxygen scavenging reaction in the scavenger channel was defined by specifying a reaction rate of 0.0577 mol/(m³·s) in the "Reaction" node. "Inflow" boundary conditions with specified flow rates were applied at the channel inlets, while "outflow" conditions were applied at the outlets. With these settings, oxygen transport within the PDMS and channels was simulated using a stationary solver.

A numerical model was employed to simulate oxygen profiles within the chemostat microfluidic chip under varying detector positions and oxygen supply conditions (**Extended Data Fig. 3b & c**), providing a computational reference for interpreting experimental measurements [17].

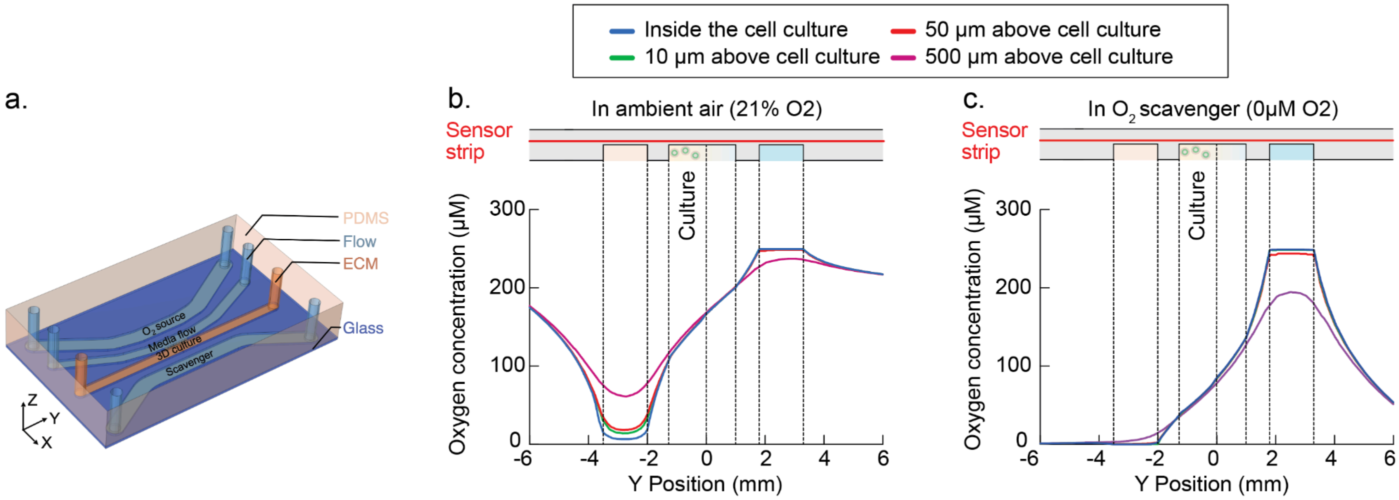

Extended Data Note 2 Fig. 1| COMSOL simulation demonstrating that scavenger-submerged chips are essential to achieve physiologically relevant hypoxia. a. Multi-channel microfluidic PDMS chip modeled in the COMSOL simulation. **b.** Simulated oxygen concentration across the entire PDMS chip exposed to ambient air. Oxygen levels within the cell culture region spanning ~100 µM to ~180 µM. **c.** Simulated oxygen concentration when the chip is submerged under sodium sulfite oxygen scavenger, where cell culture region spans ~30 µM to ~80 µM. **b&c.** Both simulations assume a 20 µL/min water flow as the oxygen source.

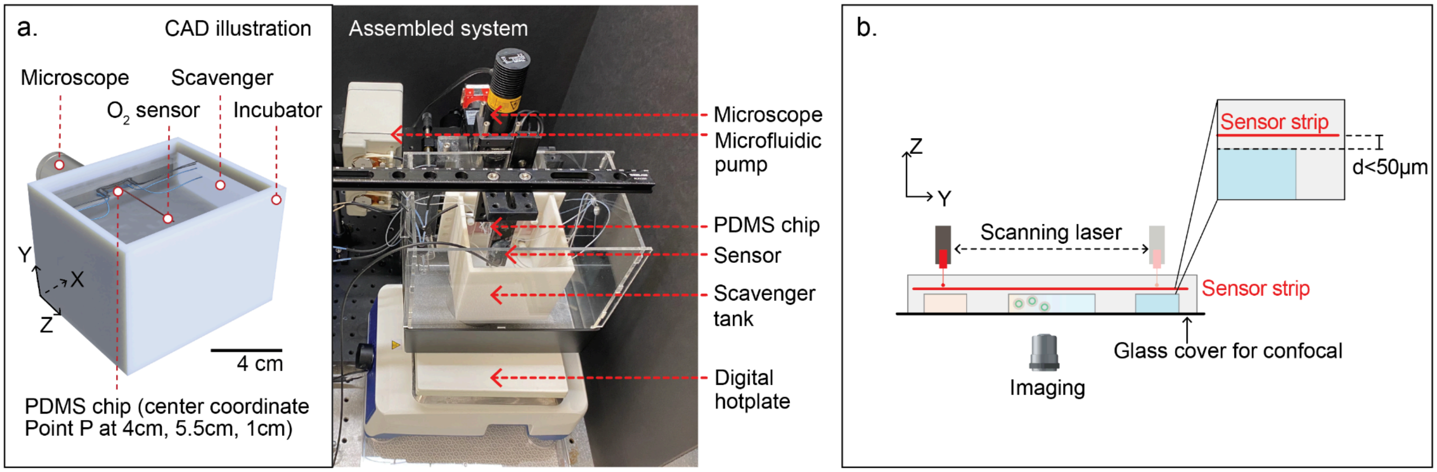

Extended Data Fig. 1| Chemostat system enables coupled real-time live-cell imaging and adjustable hypoxia profiling. a. Photograph of the experimental setup, showing the xyz-motorized stage, fiber-optic oxygen sensor, microfluidic pump, PDMS culture chip, imaging optics and temperature controller. **b.** Schematic of chemostat chip, illustrating back-side confocal access and PDMS-side oxygen scanning via a sensor strip embedded during PDMS casting less than 200μm from the cell culture for in situ oxygen measurement.

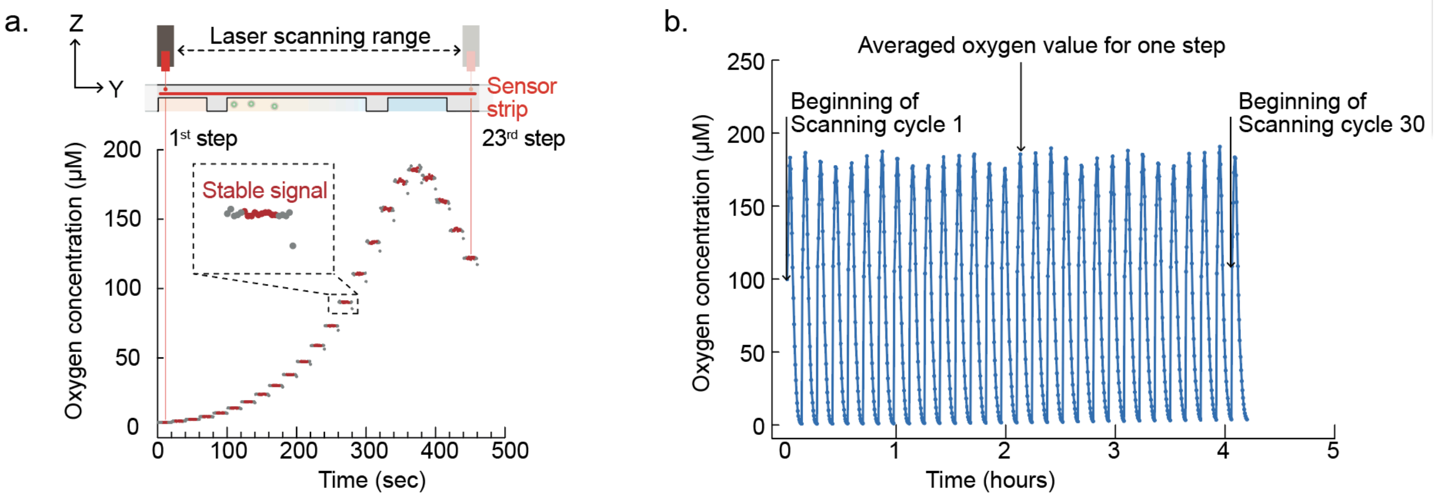

Extended Data Fig. 2| Continuous *in situ* profiling of oxygen gradients. a. Raw data from the fiber-optic sensor measured across 23 positions of the chemostat chip (step size 1 mm). At each position, the sensor dwells for 20 s, generating 20 measurements; the middle 10 stabilized readings are averaged to determine the local oxygen concentration. **b.** Sequential full-chip scans performed every 7 min produce cyclic oxygen profiles, demonstrating sustained gradient stability.

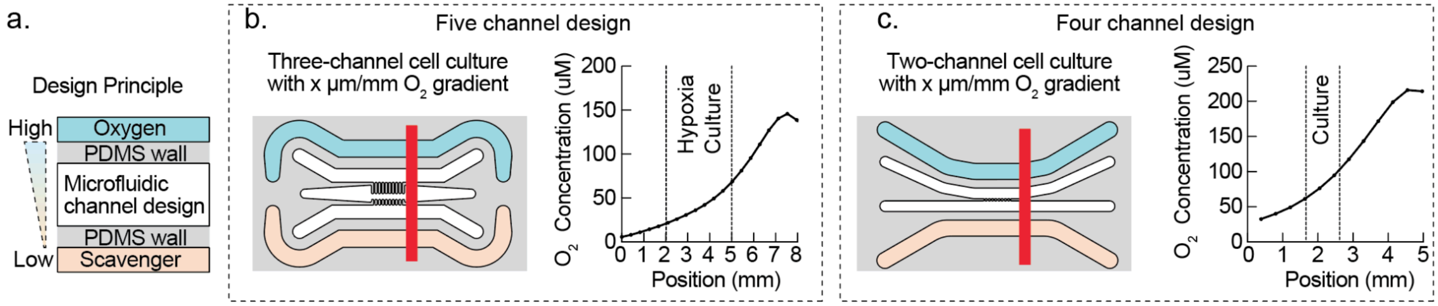

Extended Data Fig. 3| Chemostat chip design principle enables generation of oxygen gradients in diverse microfluidic devices. a. Schematic of the design principle: submerging the PDMS chip under sodium sulfite scavenger creates a hypoxic condition, requiring only a single oxygen-input channel and allowing straightforward integration with existing channel-based microfluidic systems. Oxygen and scavenger channels are physically separated from the cell culture channels with PDMS barrier walls to allow flow rate in the oxygen source channel to be independently controlled without inducing shear stress on the cultured cells; **b.** Five-channel configuration with three central culture channels, a common multiculture layout used in droplet generation, organ-on-chip and cell-assay applications, readily adapted to chemostat hypoxia; **c.** Four-channel design used in this study, wherein reduced spacing between the oxygen source and sink channels produces a steeper gradient compared to the five-channel layout.

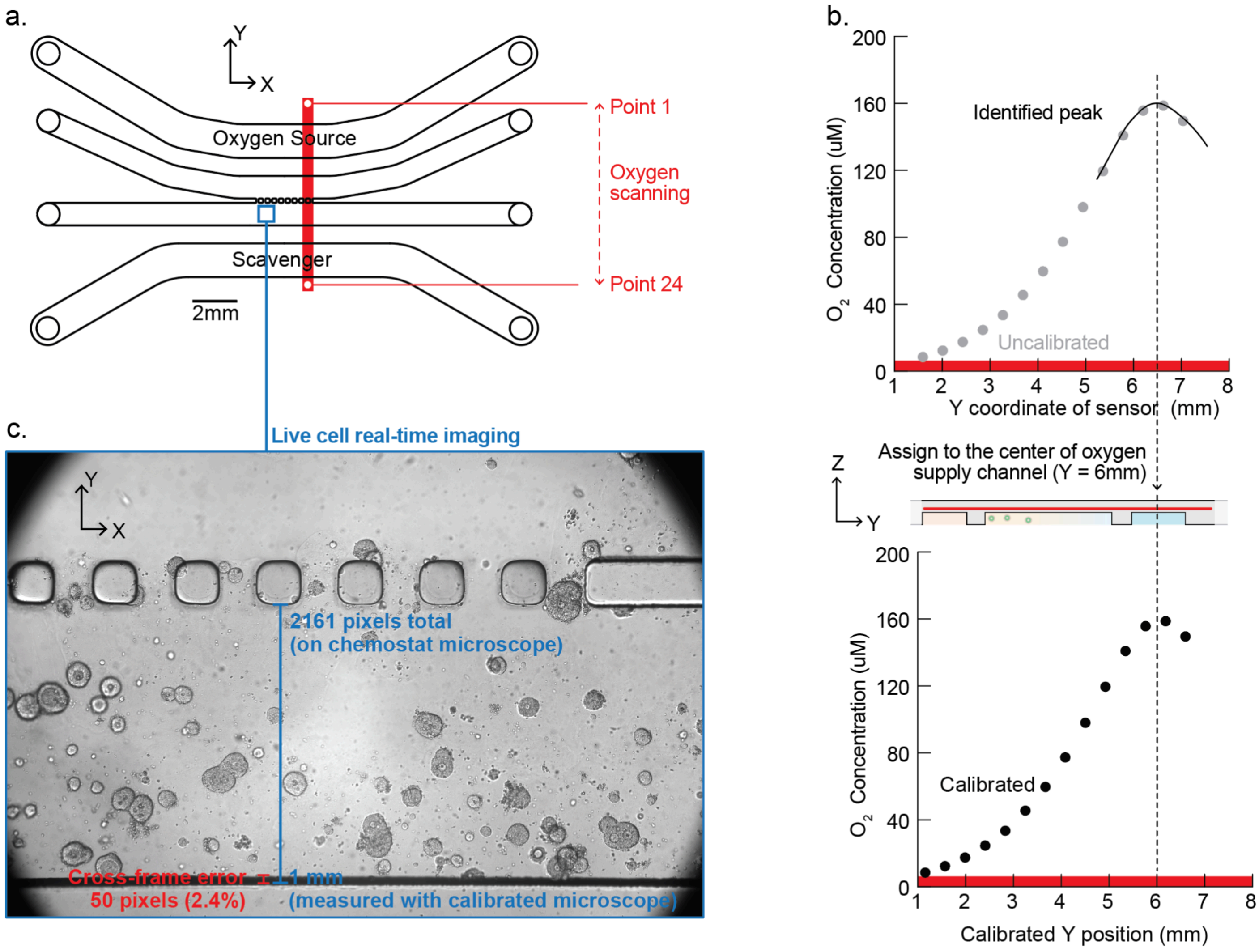

Extended Data Fig. 4| Chemostat enables precise alignment of oxygen gradients with real-time live-cell microscopy. a. Overlay of in situ oxygen measurements and live-cell imaging on the chemostat chip. **b.** MATLAB routines detect the peak oxygen level, corresponding to the center of the oxygen-supply channel, to map sensor coordinates (uncalibrated) onto chip coordinates (calibrated). **c.** Bright-field images provide intrinsic landmarks for direct registration to chip coordinates and correlation with the oxygen gradient; focus drift across frames introduces <5% alignment error (2.4% in this example).

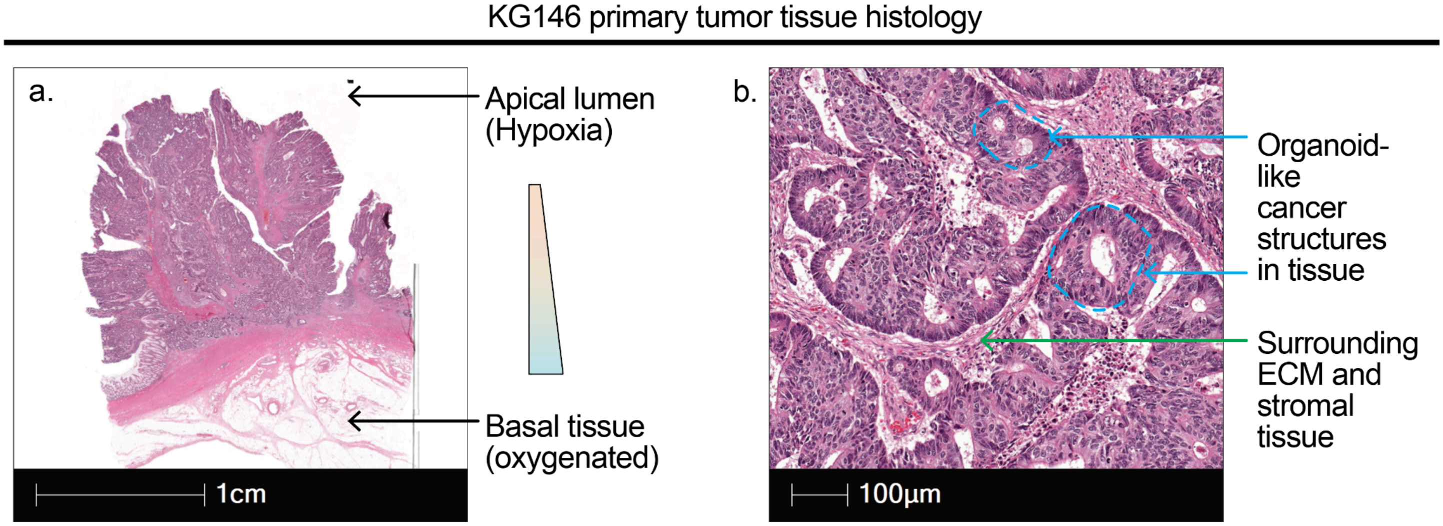

Extended Data Fig. 5 | Histological organization of patient KG 146 primary colorectal tumor. a. Low-magnification H&E-stained section illustrating the apical–basal orientation of the tumor *in situ*, aligned with the intestinal axis. **b.** High-magnification image revealing multiple glandular epithelial structures resembling organoids, each encapsulated within extracellular matrix and surrounded by stromal tissue.

a. Oxygen profile based on the **mode** reported oxygen consumption value
O_2 gradient = 20 μM/mm
(Rc = 2e-4 mol/(m^3·s)

Oxygen profile based on the **maximum** reported oxygen consumption value
O_2 gradient = 20 μM/mm
(Rc = 6e-4 mol/(m^3·s)

Oxygen profile based on the **mode** reported oxygen consumption value
O_2 gradient = 10 μM/mm
(Rc = 2e-4 mol/(m^3·s)

Oxygen profile based on the **maximum** reported oxygen consumption value
O_2 gradient = 10 μM/mm
(Rc = 6e-4 mol/(m^3·s)

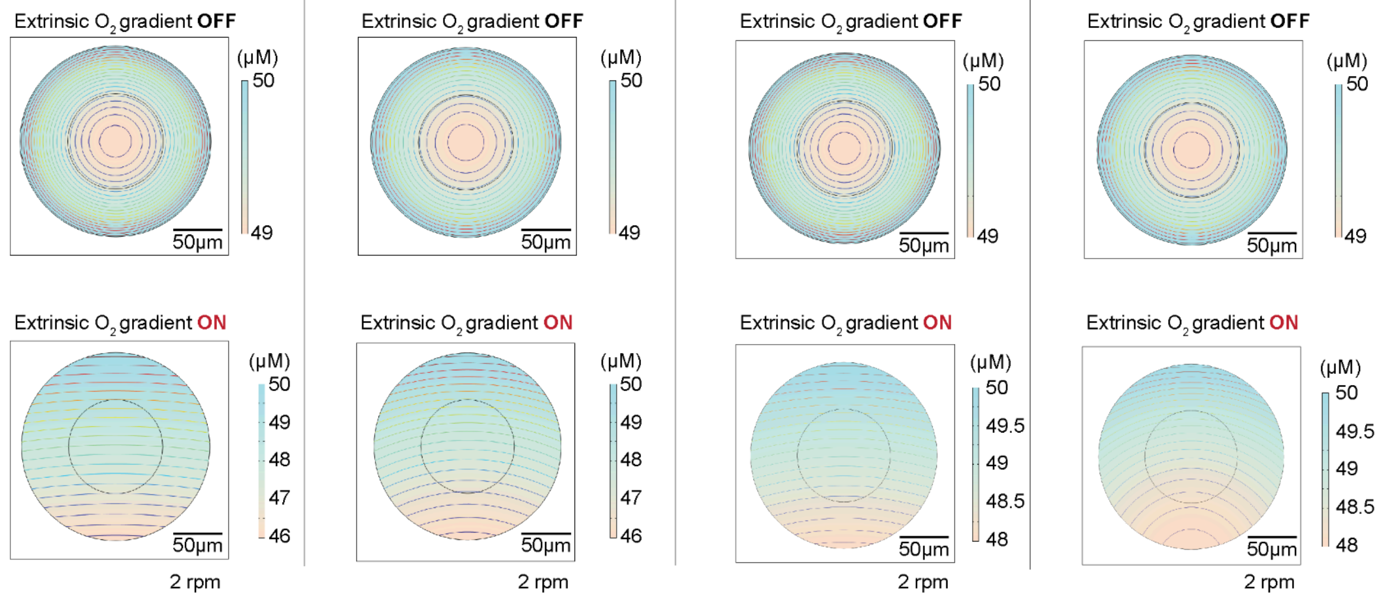

b. Change of oxygen flux at key location on x-y plane

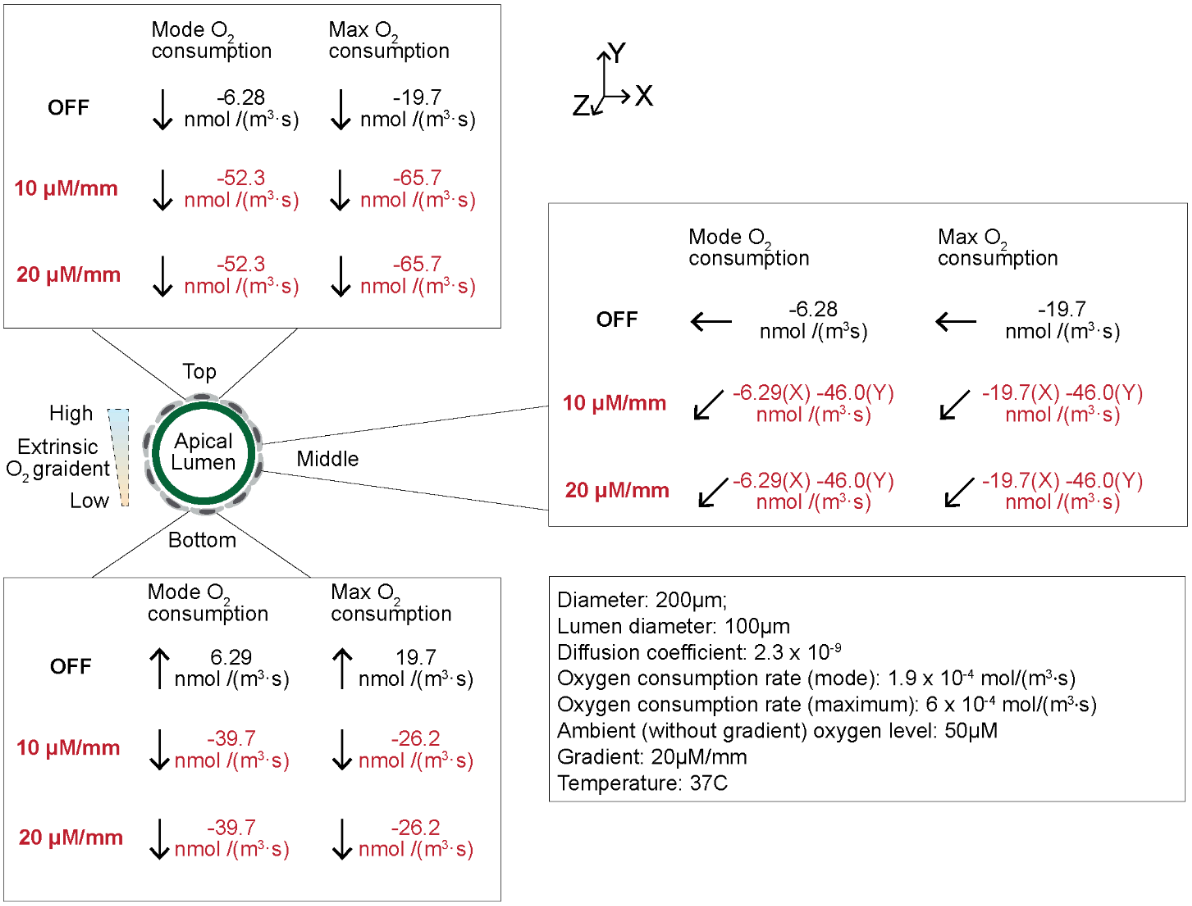

	Mode O_2 consumption	Max O_2 consumption
OFF	↓ -6.28 nmol /(m^3·s)	↓ -19.7 nmol /(m^3·s)
10 μM/mm	↓ -52.3 nmol /(m^3·s)	↓ -65.7 nmol /(m^3·s)
20 μM/mm	↓ -52.3 nmol /(m^3·s)	↓ -65.7 nmol /(m^3·s)

	Mode O_2 consumption	Max O_2 consumption
OFF	← -6.28 nmol /(m^{3}s)	← -19.7 nmol /(m^3·s)
10 μM/mm	↙ -6.29(X) -46.0(Y) nmol /(m^3·s)	↙ -19.7(X) -46.0(Y) nmol /(m^3·s)
20 μM/mm	↙ -6.29(X) -46.0(Y) nmol /(m^3·s)	↙ -19.7(X) -46.0(Y) nmol /(m^3·s)

	Mode O_2 consumption	Max O_2 consumption
OFF	↑ 6.29 nmol /(m^3·s)	↑ 19.7 nmol /(m^3·s)
10 μM/mm	↓ -39.7 nmol /(m^3·s)	↓ -26.2 nmol /(m^3·s)
20 μM/mm	↓ -39.7 nmol /(m^3·s)	↓ -26.2 nmol /(m^3·s)

Diameter: 200μm;
Lumen diameter: 100μm
Diffusion coefficient: 2.3 x 10^{-9}
Oxygen consumption rate (mode): 1.9 x 10^{-4} mol/(m^3·s)
Oxygen consumption rate (maximum): 6 x 10^{-4} mol/(m^3·s)
Ambient (without gradient) oxygen level: 50μM
Gradient: 20μM/mm
Temperature: 37C

Extended data Fig. 6| Oxygen profile of cultured organoid. a. COMSOL simulation of oxygen gradient within organoids cultured with or without extrinsic oxygen gradient, using mode and the maximum of reported oxygen consumption of cells reported in literature. **b.** Calculated change of oxygen flux at key locations of each organoid, according to COMSOL simulation.

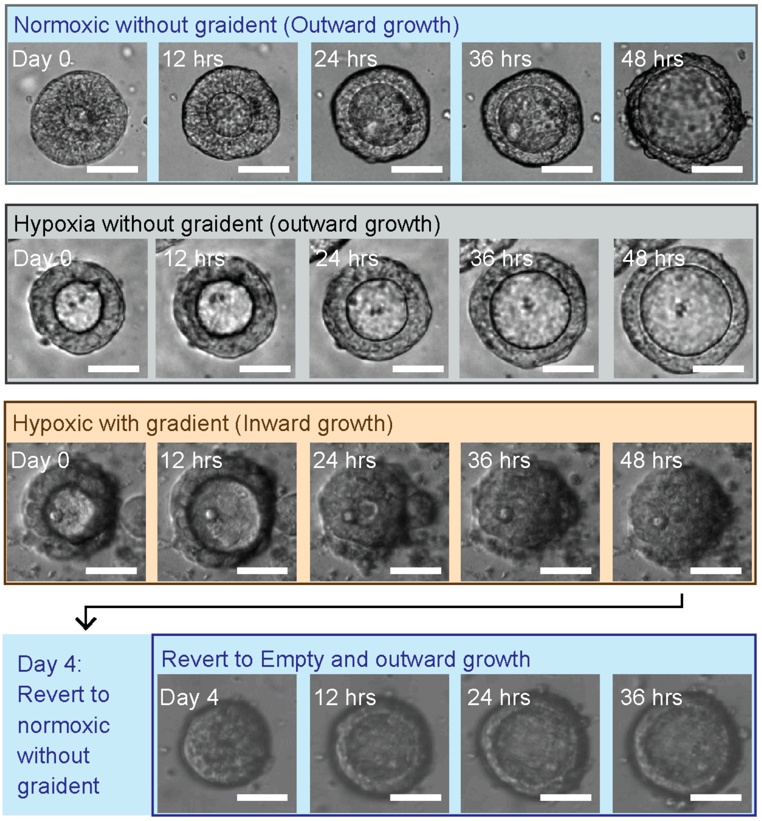

Extended Data Fig. 7| Cancer organoids revert to cystic morphology after removal of oxygen gradient.

Methods

Organoid samples. Human organoid generation and culture was performed as previously described8. Briefly, patients undergoing colorectal resection and metastasectomy at MSKCC were identified by chart review. Informed consent for bio-specimen tissue collection of primary tumor was obtained through MSK IRB protocols 06-107, 12-245, 14-244 or 22-404. Freshly resected surgical tissue in surplus of clinical diagnostic requirements was processed for organoid generation. Human tumor organoids were maintained in Matrigel and cultured in HISC media (Advanced DMEM/F12 (AdDF12; Thermo Fisher Scientific), GlutaMAX (2 mM, Thermo Fisher Scientific), HEPES (10 mM, Thermo Fisher Scientific), N-acetyl-l-cysteine (1 mM, Sigma-Aldrich), B27 supplement with vitamin A (Thermo Fisher Scientific), Primocin (100 µg ml−1, InvivoGen), EGF (50 ng ml−1, Peprotech), Noggin (100 ng ml−1, Peprotech), A8301 (500 nM, Sigma-Aldrich), FGF2 (50 ng ml−1, Peprotech), IGF-I (100 ng ml−1, Peprotech). All animal procedures were approved by the Institutional Animal Care and Use Committee (IACUC) of Memorial Sloan Kettering Cancer Center. Normal mouse organoids were derived from C57BL/6J mice (strain 000664, Jackson Laboratories). Colons were dissected, flushed with PBS to remove faecal content, opened longitudinally, and cut into ~1 cm segments. Tissues were incubated in dissociation buffer (PBS with 8 mM EDTA, 0.5 mM DTT, and 10 U/mL DNase I (Roche 04716728001)) at 4C with gentle shaking for 60 minutes. Crypts were detached by vigorous shaking, pelleted, and further dissociated with TrypLE (Thermo Fisher Scientific). The resulting cell suspension was plated in and cultured in mouse HISC media (Advanced DMEM/F12 (AdDF12; Thermo Fisher Scientific), GlutaMAX (2 mM, Thermo Fisher Scientific), HEPES (10 mM, Thermo Fisher Scientific), N-acetyl-l-cysteine (1 mM, Sigma-Aldrich), B27 supplement with vitamin A (Thermo Fisher Scientific), N2 Supplement (ThermoFisher Scientific), Primocin (100 µg ml−1, InvivoGen), EGF (50 ng ml−1, Peprotech), murine Noggin (100 ng ml−1, Peprotech), A8301 (500 nM, Sigma-Aldrich), FGF2 (50 ng ml−1, Peprotech), IGF-I (100 ng ml−1, Peprotech),NGS-WNT (1 nM, ImmunePrecise N0001), and murine R-spondin 1 (1 µg mL-1, Peprotech). Established organoids were maintained in 6 well plates, dissociated to single cells (TrypLE, Thermo Fisher Scientific) for chemostat seeding. Organoids were routinely tested for mycoplasma contamination (MycoALERT PLUS detection kit, Lonza).

Lentiviral generation and transduction. Lentivirus was generated as previously described (PMID: 27246018). Briefly, pLenti-HRE-dUnaG (UnaG) was a gift from Roland Friedel (Addgene plasmid # 124372 ; http://n2t.net/addgene:124372 ; RRID:Addgene_124372) and pLV 4xSTAR-mScarletI-NLS-blast (STAR) was a gift from Hugo Snippert (Addgene plasmid # 136260 ; http://n2t.net/addgene:136260 ; RRID:Addgene_136260). HEK293T cells (ATCC) were cultured in DMEM supplemented with 10% FBS, GlutaMAX (2 mM, Thermo Fisher Scientific) and penicillin–streptomycin (100 IU ml−1, 0.1 mg ml−1, Thermo Fisher Scientific). HEK29T cells were transfected with 2nd generation packaging and envelope plasmids PAX (Addgene#12259) and MD2G (addgene), and UnaG or STAR plasmids. Media was replenished after 24 hours, and media containing virus was collected at 72 hours post transfection. Virus was concentrated with Lenti-X Concentrator (Takara Bio) overnight at 4C. Organoids were transduced with UnaG and STAR reporter virus, and antibiotic selection with puromycin or blasticidin, respectively, was initiated 72 hours after transduction. Organoid reporter lines were considered established after 3 passages. All cells were routinely tested for mycoplasma contamination (MycoALERT PLUS detection kit, Lonza).

COMSOL simulation. Numerical simulation was performed using finite element method (FEM)-based computational modeling software, COMSOL Multiphysics 5.4. Simulations were developed to solve the oxygen profiles in the fluidic cell-culture microchannel [16]. The COMSOL "Laminar Flow" interface with FEM formulations of the transport equation was applied to the 3D solution domain. This domain is a section of fluid in the channel (domain height: 0.25 mm, domain width: 1 mm). For the Materials selection, we used water, liquid to model the fluid inside channels, and PDMS to model the remaining PDMS structure. An "outlet" condition was applied to the two ends of the channel. And, the boundary conditions were set to "no slip" at the bottom and sides of the channel. The model was solved by a "stationary" solver to get the steady streaming pattern in the fluid domain.

Microfluidic device fabrication. The microfluidic device consisted of two parts: a microscope glass slide (75 mm × 25 mm × 1 mm, Fisher Scientific Inc.) and a PDMS channel layer with an embedded oxygen sensor.

The microfluidic channel was designed using AutoCAD and printed onto a photomask. The pattern was transferred onto a 4-inch silicon wafer via standard photolithography, using SU-8 2150 photoresist to produce microchannels with a height of approximately 200 µm. Polydimethylsiloxane (PDMS; Sylgard 184, Dow Corning) was prepared at a 10:1 base-to-curing-agent ratio and used to cast the device.

To integrate the oxygen sensor, a multilayer PDMS casting approach was employed. A small volume of PDMS was first poured onto the mold and spin-coated to form a ~250 µm layer, resulting in a ~50 µm PDMS layer above the channel ceiling after partial curing. At this stage, a pre-fabricated oxygen sensor strip (TROXSP5, PyroScience GmbH, Germany) was carefully positioned onto the sensing region. The sensor strip was trimmed into a 2 mm × 10 mm rectangle from a sensor patch originally supplied as a 10 mm × 10 mm square, and was aligned under a stereomicroscope to ensure consistent placement across devices.

After sensor placement, additional PDMS was poured to reach a total thickness of approximately 500 µm. The PDMS was then fully cured and peeled from the mold. Inlet and outlet ports were punched for tubing connections, and the PDMS layer was bonded to the glass slide using oxygen plasma treatment (AutoGlow 200, Glow Research)..

Chemostat system fabrication. The chemostat system included a 3D-printed scavenger tank mounted against the optical setup. Media perfusion is controlled by a VWR peristaltic pump. The scavenger tank is heated via water bath and hot plate with a safety shutoff at 37 °C to maintain stable temperatures. A custom LabVIEW program integrated control of the scanning stage, pump, light source, and imaging system. Brightfield imaging was performed using a VM-2 video microscope with integrated camera and 10X objective, enabling time-lapse capture of organoid cultures during oxygen gradient formation.

Oxygen Sensing and Gradient Profiling. Dissolved oxygen in the microfluidic chemostat device was measured using a contactless optical sensor system (PyroScience GmbH) comprising TROXSP5 sensor strips, a SPFIB-BARE optical fiber, and a FireSting-O2 meter. Sensor strips (2 mm × 10 mm) were embedded <200 µm from the organoid culture region and spanned the channel width. Fluorescence signals were converted to oxygen concentrations using Pyro Workbench software. Sensors were calibrated monthly using air-saturated water and 10 g/L sodium sulfite.

The optical fiber was mounted on a motorized XY stage (Thorlabs LTS150), controlled via LabVIEW, to scan oxygen along the Y-axis. Scanning parameters, including step size, number of steps, and dwell time, were customizable; typically, 22–23 positions were sampled at 0.4 mm intervals. At each location, 20 data points were collected over 20 seconds; the first and last 5 were discarded to minimize motion artifacts, and the middle 10 were averaged. Each scan took ~7 minutes, enabling continuous profiling (~7 scans/hour).

Immunocyto staining and confocal imaging. Organoids cultured under chemostat conditions were fixed *in situ* to preserve gradient-induced phenotypes. Briefly, live P146 organoids were incubated with 200 nM Mitotracker FM Deep Red (Thermo Fisher Scientific) in the chemostat for 30 minutes, washed twice with media, and then fixed with 4% paraformaldehyde in PBS for 30 minutes at room temperature. After fixation, samples were washed three times with PBS, permeabilized in 0.1% Triton X-100 in PBS for 10 minutes, and blocked in 5% bovine serum albumin (BSA) in PBS for 1 hour. F-actin was labeled by incubating with Alexa Fluor 488–conjugated phalloidin (Invitrogen; 1:200 in 1% BSA/PBS) and nuclei were counterstained with DAPI (1 µg mL^{-1}; Thermo Fisher Scientific). Following three PBS washes, the PDMS chips remained filled with PBS until imaging. All antibodies and dyes were diluted in 1% FCAs buffer, and wash steps consisted of gentle flushing with PBS. Whole-mount protocols (e.g., fixation in 4% PFA and permeabilization in Triton X-100) were adapted from established organoid immunofluorescence methods2[18]. Confocal images were acquired on either a Leica SP8 or a Nikon Ti inverted confocal microscope. Excitation/emission settings were as follows: DAPI, 405 nm/425–475 nm; Alexa 488 (phalloidin), 488 nm/500–550 nm; Mitotracker Deep Red, 640 nm/655–705 nm.

Image processing. All confocal datasets were processed and quantified in ImageJ. Z-stacks were imported as hyperstacks and subjected to a maximum-intensity projection. Lumen size was quantified by selecting enclosed regions of low F-actin signal or high contrast boundary in the bright field. The "Analyze" function was used to measure lumen area. Cell-covered area was determined by subtracting lumen area from the total cell size. All threshold levels and ROI settings were held constant across experimental groups. Quantification was performed from at least three independent chemostat runs.

Patient pathology. Archival formalin-fixed, paraffin-embedded (FFPE) clinical tissue blocks for immunostaining were identified by database search and chart review of patients who had signed pre-procedure informed consent to MSK IRB protocols 06-107, 12-245, 14-244 or 22-404 for biospecimen collection. Histopathological data interpretation were overseen by an expert gastrointestinal pathologist as previously described8.Tissue sectioning and hematoxylin and eosin (H&E) staining were performed by the MSKCC Molecular Cytology Core. For immunofluorescence (IF) staining, 5 um tissue sections were dewaxed (Histo-clear, cat# 50-899-90147), rehydrated, and steamed in antigen retrieva buffer (Abcam, ab93678) for 20 minutes. Cooled slides were washed twice with IF buffer (0.2% Triton X-10, 0.05% Tween, in PBS), blocked in 10% normal goat serum (Invitrogen, 50062Z) for 20 minutes, and incubated with primary mouse anti-TOMM20 antibody (1:100, Abcam, ab56783) diluted in 10% normal goat serum overnight at 4C. Following primary antibody incubation, slides were washed twice with IF buffer, incubated with TrueBlack™ Lipofuscin Autofluorescence Quencher (GoldBio, TB-250-1) diluted in 70% ethanol. After subsequent washes with 70% ethanol and IF buffer, slides were incubated with 594 anti-rabbit antibody (1:400, Invitrogen, A11012) for 1 hour at room temperature, washed three times with IF buffer and one time with cold DPBS. Slides were mounted using medium containing DAPI (Novus Biologics, H-1200-NB) and stored overnight at 4C prior to imaging on a Pannoramic Scanner (3DHistech, Budapest, Hungary) using a 40x/0.95NA objective.

Statistical analysis. The results are shown as mean ± standard error of the mean (SEM). To determine the statistical significance of the differences between the experimental groups, two-tailed unpaired Student's t tests were performed using the Prism 10 software (GraphPad), as indicated in the figure. Sample sizes were based on experience and experimental complexity, but no methods were used to determine normal distribution of the samples. Differences reached significance with p values < 0.05 (*p* values noted in figures). The figure captions contain the number of independent experiments or mice per group that were used in the respective experiments.

Reporting Summary

Further information on research design is available in the Nature Research Reporting Summary linked to this article.

Data availability

The authors declare that all data supporting the findings of this study are available within the paper and its Supplementary Information. Source data for the primary- sample figures are available.

Code availability

Custom LabView program and Matlab image processing code is available in the supplemental information.

References

1. Kather, J. N. *et al.* Identification of a characteristic vascular belt zone in human colorectal cancer. *PLoS One* **12**, e0171378 (2017).
2. Castro-Poças, F. M., Dinis-Ribeiro, M., Araújo, T. P. & Pedroto, I. Echoendoscopic characterization of the human colon. *Rev. Esp. Enferm. Dig.* **107**, 469–475 (2015).
3. Kachlik, D., Baca, V. & Stingl, J. The spatial arrangement of the human large intestinal wall blood circulation. *J. Anat.* **216**, 335–343 (2010).
4. Zhdanov, A. V. *et al.* Quantitative analysis of mucosal oxygenation using ex vivo imaging of healthy and inflamed mammalian colon tissue. *Cell. Mol. Life Sci.* **74**, 141–151 (2017).
5. Schwerdtfeger, L. A., Nealon, N. J., Ryan, E. P. & Tobet, S. A. Human colon function ex vivo: Dependence on oxygen and sensitivity to antibiotic. *PLoS One* **14**, e0217170 (2019).
6. Zheng, L., Kelly, C. J. & Colgan, S. P. Physiologic hypoxia and oxygen homeostasis in the healthy intestine. A Review in the Theme: Cellular Responses to Hypoxia. *Am. J. Physiol. Cell Physiol.* **309**, C350–60 (2015).
7. Vaupel, P., Kallinowski, F. & Okunieff, P. Blood flow, oxygen and nutrient supply, and metabolic microenvironment of human tumors: a review. *Cancer Res.* **49**, 6449–6465 (1989).
8. Zhang, L. *et al.* Partial oxygen pressure affects the expression of prognostic biomarkers HIF-1 alpha, Ki67, and CK20 in the microenvironment of colorectal cancer tissue. *Oxid. Med. Cell. Longev.* **2016**, 1204715 (2016).
9. Kamphuis, J. B. J., Mercier-Bonin, M., Eutamène, H. & Theodorou, V. Mucus organisation is shaped by colonic content; a new view. *Sci. Rep.* **7**, 8527 (2017).
10. Johansson, M. E. V. *et al.* Bacteria penetrate the inner mucus layer before inflammation in the dextran sulfate colitis model. *PLoS One* **5**, e12238 (2010).
11. The absorption of oxygen into sodium sulphite solution. *Chemical Engineering Science* **17**, 411–421 (1962).
12. Hui, P. K. & Palmer, H. J. Uncatalyzed oxidation of aqueous sodium sulfite and its ability to simulate bacterial respiration. *Biotechnol Bioeng* **37**, 392–396 (1991).
13. Shirure, V. S. *et al.* Quantitative design strategies for fine control of oxygen in microfluidic systems. *Lab Chip* **20**, 3036–3050 (2020).
14. Experimental study of oxygen diffusion coefficients in clean water containing salt, glucose or surfactant: Consequences on the liquid-side mass transfer coefficients. *Chemical Engineering Journal* **165**, 758–768 (2010).
15. Rasmussen, H. N. & Rasmussen, U. F. Oxygen solubilities of media used in electrochemical respiration measurements. *Anal Biochem* **319**, 105–113 (2003).
16. Zhang, J. *et al.* A solution to the biophysical fractionation of extracellular vesicles: Acoustic Nanoscale Separation via Wave-pillar Excitation Resonance (ANSWER). *Sci. Adv.* **8**, eade0640 (2022).
17. Chen, C. *et al.* Acoustofluidic rotational tweezing enables high-speed contactless morphological phenotyping of zebrafish larvae. *Nat Commun* **12**, 1118 (2021).
18. Moorman, A. *et al.* Progressive plasticity during colorectal cancer metastasis. *Nature* **637**, 947–954 (2024).